Copyright © 2011 Tech Science Press CMES, vol.71, no.4, pp.363-395, 2011

A novel MLPG-Finite-Volume Mixed Method for Analyzing Stokesian Flows & Study of a new Vortex Mixing Flow

Ruben Avila [1], **Zhidong Han** [2], **Satya N. Atluri** [3]

Abstract: The two dimensional steady state Stokes equations are solved by using a novel MLPG-Mixed Finite Volume method, that is based on the independent meshless interpolations of the deviatoric velocity strain tensor, the volumetric velocity strain tensor, the velocity vector and the pressure. The pressure field directly obtained from this method does not suffer from the malady of checker-board patterns. Numerical simulations of the flow field, and trajectories of passive fluid elements in a new complex Stokes flow are also presented. The new flow geometry consists of three coaxial cylinders two of smaller diameter, that steadily rotate independently, inside a third one of elliptical cross section, whose wall slides at a constant angular speed. We show, by performing detailed comparisons with analytical solutions, that the present mixed-MLPG method, coupled with an algorithm to track passive massless fluid elements, provides accurate results for the pressure and velocity fields, and for their spatial derivatives along the streamlines of the flow domain.

Keywords: Meshless Local Petrov-Galerkin approach (MLPG), Chaotic advection, Stokesian flows.

1 Introduction

Even though the Stokesian flows constitute a great simplification of the Navier-Stokes flows, they have been successfully used to model creeping flows that are present in nature as well as in industry. The development and optimal design of microfluidics devices, over the past two decades, have been based on the solution

[1] Departamento de Termofluidos, Facultad de Ingeniería, Universidad Nacional Autónoma de México, Mexico D.F., C.P. 04510, ravila@servidor.unam.mx, Center for Aerospace Research & Education, University of California, Irvine.
[2] Center for Aerospace Research & Education, University of California, Irvine.
[3] Center for Aerospace Research & Education, University of California, Irvine, satluri@uci.edu.

of the Stokes equations, see Stremler, Haselton, and Aref (2004). The steady state velocity field, obtained by the solution of the Stokes equations, has been used to study the enhancement of mixing in laminar flows through the phenomenon of chaotic advection. Chaotic advection in Stokes flows is a subject that has been addressed by physicists, fluid dynamicists and engineers over almost three decades [Aref (1984); Chaiken, Chevray, Tabor, and Tan (1986); Jana, Metcalfe, and Otino (1994); Aref (2002)]. The technological efforts to increase the Reynolds number of the flow to become turbulent, and consequently to increase the rate of mixing of industrial high viscous flows, increase the costs enormously, see Shankar and Kidambi (2009) and references therein. Chaotic advection in the Stokes flow regime, where the transport is governed by the diffusion coefficient of the fluid, has been exploited by MEMS technology and biological applications, to accelerate the rate of mixing [Karniadakis, Beskok, and Aluru (2005)].

The majority of theoretical studies of chaotic advection have been carried out by using an analytical background velocity field (which is derived from a biharmonic stream function) that randomly advects the fluids elements [Aref and Balachandar (1986); Chaiken, Chevray, Tabor, and Tan (1986); Chaiken, Chu, Tabor, and Tan (1987)]. One of the preferred analytical solutions of the velocity field, that has been used to calculate the mixing and chaotic advection properties of time modulated Stokes flows (where a sequence of steady flows are alternated to force a time dependence of the Stokes flow) is that reported by Ballal and Rivlin (1976). Very recently Shankar and Kidambi (2009) have proposed the analytical embedding method for eigenfunction expansions, to calculate the flow field in mixers with arbitrary shape. Metcalfe, Lester, Ord, Kulkarni, Rudman, Trefry, Hobbs, Regenaur-Lieb, and Morris (2010) have proposed to use an irrotational flow with periodic orientation to efficiently generate chaotic advection, the flow field in this case is the analytical solution of a dipole potential flow. Along the history of chaotic advection, several theoretical results, concerning the parameters that characterize the degree of mixing, such as the Poincaré sections or Liapunov exponents have been successfully verified by experimental techniques [Chaiken, Chevray, Tabor, and Tan (1986); Jana, Metcalfe, and Otino (1994); Price, Mullin, and Kobine (2003); Metcalfe, Lester, Ord, Kulkarni, Rudman, Trefry, Hobbs, Regenaur-Lieb, and Morris (2010)]. Several numerical methods have also been used to calculate the background Stokes flow field. A whole review of the many papers dealing with the numerical solution of the Stokes equations with application to chaotic advection is almost impossible. So we will just mention some of the papers in which different numerical approaches have been used. Jana, Metcalfe, and Otino (1994) used the boundary integral equation method to obtain the steady state flow field in a vortex mixing flow. Anderson, Ternet, Peters, and Meijer (2006) used the spectral element method to calculate the steady state three dimensional velocity field in a lid-driven cubical cavity. The fictitious-domain coupled with the finite element method was used to calculate the steady state two dimensional flow field in a lid-driven cavity, and in a serpentine channel, in the presence of solid particles [Hwang, Anderson, and Hulsen (2005); Kang, Hulsen, Anderson, den Toonder, and Meijer (2007)]. Many numerical techniques have also been used to calculate the basic flow field when inertial effects are taken into account (finite element method, finite volume method, spectral element method and mapping methods), see Wang, Feng, Otino, and Lueptow (2009) and references therein.

By using a numerical approach, it is possible to calculate more complex mixing vortex flows in which analytical solutions are not available. An accurate background velocity field is the starting point of reliable chaotic advection studies. Therefore an efficient and accurate algorithm for the solution of the flow field must be used.

In this paper the two dimensional steady state Stokes equations are solved by using a novel Meshless Local Petrov Galerkin (MLPG) finite-volume mixed numerical method. For a basic description of the MLPG method, see Atluri and Zhu (1998); Atluri and Shen (2002a); Atluri and Shen (2002b); Atluri (2004), and for mixed MLPG methods in solid mechanics, see Atluri, Han, and Rajendran (2004). The present mixed method for Stokesian flows is based on the independent meshless interpolation of the velocity vector, the deviatoric velocity strain tensor, the volumetric velocity strain and the pressure, using the Moving Least Squares (MLS) interpolation over randomly distributed points (nodes) in the flow domain. The present method does not involve any Lagrange multipliers, and hence bypasses the LBB type stability conditions [see, for instance Brezzi and Fortin (1991), and Ying and Atluri (1983)]. It is well known that special techniques, such as staggered grids, segregated algorithms, or lower order interpolation polynomials for the pressure field, must be used in the existing numerical methods, to satisfy the incompressibility constraint, and to avoid the checkerboard distribution of the pressure field. In the present study, the novel MLPG method is used to enforce the incompressibility condition in a strong-form, at each node (without involving any Lagrange multiplier or reduced-integration-penalty approaches) and the obtained pressure field solution is very stable and smooth. Once the background velocity field is known, it is used to calculate the smooth orbits of passive fluid elements. The newly proposed active mixer consists of three coaxial cylinders, two of smaller diameter inside a third of elliptical cross section. The two inner circular cylinders rotate independently, about their axes, to drive the flow, whereas the external elliptical housing remains stationary, however its wall slides with a constant angular velocity, hence the tangential velocity that drives the internal flow, is a function of the polar radius of the ellipse. The elliptical shape of the outer cylinder provides not only a variant in the geometry of vortex mixing flows previously reported in the literature, but also a variant in the boundary condition on the outer channel that drives the fluid. The purpose of the new mixer is to split the flow into several flow streams, with the objective of increasing the mixing surface area. We study the capabilities of the active mixer to split the flow field in terms of the forcing parameter (angular speed of the three cylinders) while the geometry is kept fixed. In previous studies, mixers, constituted by three cylinders, in which the outer circular cylinder rotates about its axis, with constant angular velocity, have been analyzed [Jana, Metcalfe, and Otino (1994); Price, Mullin, and Kobine (2003)]. We show that the new geometry produces a great variety of complex Stokes flows.

This paper is organized as follows. In Sect. 2, the present MLPG Mixed Finite-Volume method is described. The MLS numerical method is used to digitally generate the trial functions of the independent variables of the flow field (the velocity vector, deviatoric velocity strain tensor, volumetric velocity strain, and pressure), and the interpolation functions to accurate evaluate the velocity of the fluid at the location of the passive tracer along its smooth orbit. In Sect. 3 we present the results for steady state Stokes flows in eccentric cylinders. A comparison of the numerical results with the analytical solution given by Ballal and Rivlin (1976) is carried out. In Sect. 3 we also show the flow field and the pathlines (streamlines) of passive traces in the new complex Stokes vortex mixing flow. Finally in Sect. 4 we present the concluding remarks.

2 The Meshless Local Petrov Galerkin (MLPG) Mixed-Finite-Volume method

In this section, we sketch the present method of analysis of the Stokesian flows. We first give a brief historical sketch of the various methods [mostly finite element and finite volume] developed in earlier literature. Thereby, we motivate on present approach of the Meshless Local Petrov Galerkin (MLPG) Mixed-Finite-Volume method for analysing Stokesian incompressible flows. We consider an incompressible viscous fluid in a domain with spatial coordinates x_i. We use the notation: ρ the fluid density; $\overline{F}_i$ are body forces (excluding inertia) for unit mass; σ_{ij} the fluid stress; σ'_{ij} the deviatoric stress; p the hydrostatic pressure; v_i the velocities; D_{ij} the velocity strains; D'_{ij} the deviatoric velocity strain; D_{kk} the spherical part of velocity strain; $\bar{v}_i$ the prescribed velocities on a boundary segment S_v; $\bar{t}_i$ the prescribed tractions on a boundary segment S_t; and $()_{,i}$ denotes a partial derivative w.r.t. x_i. The well-known field equations governing the Stokesian flow of a Newtonian fluid are:

$$v_{i,i} = D_{kk} = 0 \qquad \text{(incompressibility)}, \tag{1}$$

$$\sigma_{ij,j} + \rho \overline{F}_i = 0; \quad \sigma_{ij} = \sigma_{ji} \quad \text{(momentum balance)}, \tag{2}$$

$$D_{ij} = v_{(i,j)} \equiv \frac{1}{2}\left(v_{i,j} + v_{j,i}\right) \quad \text{(kinematic compatibility)}, \tag{3}$$

$$\sigma_{ij} = \frac{\partial A}{\partial D_{ij}} \quad \text{(constitutive law)}, \tag{4}$$

where

$$A = A\left(p, D_{ij}\right) = -pD_{kk} + \mu D_{ij} D_{ij}, \tag{5}$$

and μ is the coefficient of viscosity. And thus,

$$\sigma_{ij} = -p\delta_{ij} + 2\mu D_{ij} = -p\delta_{ij} + 2\mu D'_{ij}, \tag{6}$$

$$\sigma_{ij} n_j = t_i = \bar{t}_i \quad \text{(traction b.c.)}, \tag{7}$$

$$v_i = \overline{v}_i \quad \text{(velocity b.c.)}. \tag{8}$$

In Eq. (7), n_i are components of a unit outward normal to S. We further note that;

$$\sigma_{ij} = -p\delta_{ij} + \sigma'_{ij}, \tag{9}$$

and thus,

$$\sigma'_{ij} = 2\mu D'_{ij} \equiv 2\mu D_{ij}. \tag{10}$$

If the velocity fields satisfy Eq. (8) a priori, and D_{ij} is defined identically through Eq. (3), conditions given by Eqs. (2) and (7), can be derived as the Euler-Lagrange equations of the stationary condition of the functional:

$$\Pi\left(p, v_i\right) = \int_V \left[-pv_{kk} + \mu v_{i,j} v_{i,j} - \rho \overline{F}_i v_i\right] dv - \int_{S_t} \bar{t}_i v_i ds. \tag{11}$$

In a large number of earlier publications [as summarized, for instance, in Bratianu and Atluri (1983)], the so-called primitive variable finite element methods, i.e., that based on assumed functions for p and v_i over each 'finite-element', were developed. However, it is also well-known that, because of the limitations of the types of interpolations which can be used for a fixed number of nodes in each element for velocities, and pressures (the number of nodes assigned to "pressure" in each element may be different from those for the velocities), the numerical stability of these primitive-variable finite-element methods are plagued by the so-called LBB conditions [as summarized for instance in Brezzi and Fortin (1991), and in Ying and Atluri (1983)]. The lack of satisfaction of these LBB conditions (which, by no means, is trivial) manifests itself in the notorious "checker-board pattern" for the computed pressures.

Many attempts to circunvent the LBB conditions were made in earlier literature (as also discussed in Bratianu and Atluri (1983)), such as the Reduced-Integration-Penalty (RIP) methods, wherein p in Eq. (11) is replaced by a "penalty-term", $p = \lambda v_{kk}$, thus leading to:

$$\Pi(\lambda, v_i) = \int_V \left[-\lambda v_{kk}^2 + \mu v_{i,j} v_{i,j} - \rho \overline{F}_i v_i\right] dv - \int_{S_t} \bar{t}_i v_i ds, \tag{12}$$

where λ is an arbitrarily large chosen penalty parameter to "tune" the solution. To obtain good results, it was found necessary to "selectively-under-integrate" numerically the penalty term λv_{kk}^2. However, while the RIP methods are very simple to implement, the fidelity of the computed pressure solution is still often very questionable. An alternative formulation based on an independent assumption of σ'_{ij} and p which, together, satisfy the momentum balance conditions in each element, and velocity field $\tilde{v}_i$ at the inter-element boundary, was used by Bratianu and Atluri (1983) and Ying and Atluri (1983). These "hybrid" methods were based on the stationary condition of the "global" functional:

$$e^*\left(\sigma'_{ij}, p, v_i\right) = \sum_n \left\{ -\int_{V_n} \frac{1}{4\mu} \sigma'_{ij} \sigma'_{ij} dv + \int_{\partial V_n} n_i \left(\sigma'_{ij} - p\delta_{ij}\right) v_i ds - \int_{S_{t_n}} \bar{t}_i v_i ds \right\}, \tag{13}$$

where V_n is the n^{th} element, and ∂V_n its boundary. This method, also suffers from the LBB conditions on the independent fields σ'_{ij}, p, and v_i (see Ying and Atluri (1983)), while many successful elements (obeying the LBB conditions) were developed in Bratianu and Atluri (1983) and very smooth solutions for pressure were obtained; without any selective reduced integration, or other remedies.

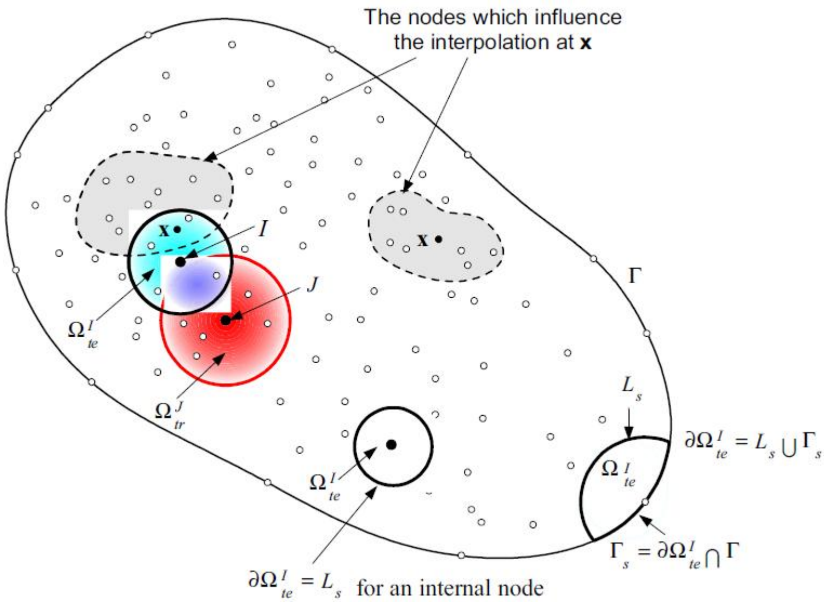

Figure 1: Scheme of the MLPG method. The global flow domain is defined as Ω with global boundary Γ. The local sub-domains Ω_s with boundary Γ_s, may overlap each other.

In this paper, we make a fundamental departure from the finite element methods based on "global variational principles" (involving the weak-forms over the entire domain V as in Eqs. (11), (12) or (13)).

We consider the fluid domain to be sprinkled with a set of arbitrarily and randomly distributed "nodes" as shown in Fig. 1. We consider a "local" interpolation, which is complete, and continuous (to any desired degree) [see Atluri (2004)]. By "locality" we mean that the value of the interpolation at any point $\mathbf{X}$ in Fig. 1 is determined uniquely only by the respective values of the interpolant at the N nodes which are in the "domain of influence" of the node $\mathbf{X}$. Such an interpolation, the Moving Least Squares interpolation, has been extensively discussed in literature, and summarized for instance in Atluri and Shen (2002b); Atluri and Shen (2002a) and Atluri (2004). Formulations of the MLPG method, for Navier-Stokes flows, using primitive variables p and v_i only, were presented in the pioneering papers by Lin and Atluri (2000) and Lin and Atluri (2001). In MLS interpolation, the interpolations for, say velocities, in the local domain Ω_S near $\mathbf{X}$, may be approximated, by using the information provided by a number of scattered nodes located at $\mathbf{X}_K$,

$K = 1...N$, in the vicinity of $\mathbf{X}$, as:

$$v_i(\mathbf{X}) = \mathbf{P}^T(\mathbf{X})\,\mathbf{a}_i(\mathbf{X}), \quad \forall \mathbf{X} \in \Omega_S, \tag{14}$$

where $\mathbf{P}^T(\mathbf{X}) = [p_1(\mathbf{X}), p_2(\mathbf{X}), ...p_m(\mathbf{X})]$ is a monomial basis of order m, and $\mathbf{a}_i(\mathbf{X})$ are vectors containing unknown coefficients (for each of the i^{th} velocity component) which are functions of $\mathbf{X}$, and whose order depends on the monomial basis. The coefficients $\mathbf{a}_i$ are determined by minimizing the weighted discrete L_2 norm:

$$\mathbf{J}_i(\mathbf{X}) = \sum_{K=1}^{N} w_K(\mathbf{X})\left[\mathbf{P}^T(\mathbf{X}_K)\,\mathbf{a}_i(\mathbf{X}) - \hat{v}_{iK}\right]^2 \equiv \; [\mathbf{P}\cdot\mathbf{a}_i(\mathbf{X}) - \hat{\mathbf{v}}_i]\,\mathbf{W}\,[\mathbf{P}\cdot\mathbf{a}_i(\mathbf{X}) - \hat{\mathbf{v}}_i], \tag{15}$$

where w_K are weight functions centered at node $\mathbf{X}_K$ and $\hat{v}_{iK}$ are the fictitious values of v_i at node $\mathbf{X}_K$. As shown in Atluri (2004), after minimizing $\mathbf{J}_i$ of Eq. (15), Eq. (14) may be written as:

$$\mathbf{v}_i(\mathbf{X}) = \mathbf{P}^T(\mathbf{X})\,\mathbf{A}^{-1}(\mathbf{X})\,\mathbf{B}(\mathbf{X})\,\hat{v}_i \equiv \sum_{K=1}^{N} \Phi^{(J)}(\mathbf{X})\,\hat{v}_i(\mathbf{X}_J), \tag{16}$$

where $\hat{v}_i(\mathbf{X}_J)$ is the fictitious nodal value of the velocity v_i and $\Phi^{(J)}(\mathbf{X})$ are the corresponding nodal trial functions centered at node $\mathbf{X}_J$. The matrices $\mathbf{A}$ and $\mathbf{B}$ in Eq. (16) are defined by [Atluri (2004)]:

$$\mathbf{A}(\mathbf{X}) = \mathbf{P}^T\mathbf{W}\mathbf{P}\,, \quad \mathbf{B}(\mathbf{X}) = \mathbf{P}^T\mathbf{W}, \quad \forall \mathbf{X} \in \partial\Omega_S. \tag{17}$$

The weight function $w_K(\mathbf{X})$ centered at node $\mathbf{X}_K$ determines the range of influence of node K, and the weight function is selected to have a compact support. A 4^{th} order spline function is used for $w_K(\mathbf{X})$ in the present study.

With this background on the local (compactly supported), complete, and continuous trial functions for any variable, such as velocity v_i, we now return to the MLPG finite-volume mixed method of the present study, following the related work for solid mechanics, reported in Atluri, Han, and Rajendran (2004).

We rewrite the equations of the Stokesian flow, instead of using the "primitive variables" (v_i and p), by using the "mixed variables" v_i, D'_{ij}, D_{kk}, and p. Thus, the equations for Stokesian flow are written as:

$$-p_{,i} + \overline{F}_i + 2\mu D'_{ij,j} = 0 \quad \text{(equilibrium)}, \tag{18}$$

$$D_{kk} = 0 \quad \text{(incompressibility)}, \tag{19}$$

$$D_{kk} = v_{k,k} \quad \text{(compatibility-1)}, \tag{20}$$

$$D'_{ij} = \frac{1}{2}\left[v_{i,j} + v_{j,i} - \frac{2}{3}v_{kk}\delta_{ij}\right] \quad \text{(compatibility-2)}. \tag{21}$$

For each of the mixed variables v_i, D_{kk}, D'_{ij} and p, we assume independent MLS approximations, at each point $\mathbf{X}$ in the domain, in terms of values at N neighbouring ('local') nodes, as:

$$v_i(\mathbf{X}) = \sum_{J=1}^{N} \Phi^{(J)}(\mathbf{X})\,\hat{v}_i^{(J)}; \quad v_i^{(J)} = v_i(\mathbf{X}_J), \tag{22}$$

$$D_{kk}(\mathbf{X}) = \sum_{J=1}^{N} \Phi^{(J)}(\mathbf{X})\,\hat{D}_{kk}^{(J)}; \quad D_{kk}^{(J)} = D_{kk}(\mathbf{X}_J), \tag{23}$$

$$D'_{ij}(\mathbf{X}) = \sum_{j=1}^{N} \Phi^{(J)}(\mathbf{X})\,\hat{D}_{ij}^{\prime(J)}; \quad D_{ij}^{\prime(J)} = D'_{ij}(\mathbf{X}_J), \tag{24}$$

$$p(\mathbf{X}) = \sum_{j=1}^{N} \Phi^{(J)}(\mathbf{X})\,\hat{p}^{(J)}; \quad p^{(J)} = p(\mathbf{X}_J). \tag{25}$$

Thus, the nodal trial function for each of the mixed variables, is the *same*, namely, $\Phi^{(J)}(\mathbf{X})$, centered at node $\mathbf{X}_J$. We satisfy the three Eqs. (18) in a "weak-sense", using a *local weak-form* over a local-sub-domain, Ω_{te}^{I}, centered at each node $\mathbf{X}_I$, using test-functions u_i, corresponding to each trial-function v_i, as:

$$\int_{\Omega_{te}^{J}} \left(-p_{,i} + \overline{F}_i + 2\mu D'_{ij,j}\right) u_i d\Omega = 0. \tag{26}$$

In this paper, we take u_i to be 'unity' over each Ω_{te}^J, thus labeling the present approach a 'finite-volume' method. The fact that the trial and test functions in the 'local weak-form' are different, the present method is labeled as the Meshless Local Petrov-Galerkin finite-volume-mixed method. When u_i=1, Eq. (26) reduces to the 'weak-form' of the equilibrium equations:

$$\int_{\Omega_{te}^J} \overline{F}_i d\Omega + \int_{\partial\Omega_{te}^J} \left(2\mu D'_{ij} n_j - p n_i\right) ds\ , \quad (i = 1,2,3), \tag{27}$$

which are simply the "force balances" on Ω_{te}^J, where $\partial\Omega_{te}^J$ is the surface of Ω_{te}^J.

In the present method we satisfy Eqs. (19)-(21) in a "strong-form" at each collocation node $\mathbf{X}_K$. Thus the "incompressibility" condition is satisfied in a "strong-form", without any Lagrange multipliers, and hence there are no LBB conditions in the present approach, which is made possible, essentially through the local meshless interpolations. The compatibility conditions for velocity strains, Eqs. (20) and (21) are also satisfied in a "strong-form" at each collocation point $\mathbf{X}_J$. When Eq. (24) is substituted in Eq. (27) we obtain:

$$\int_{\Omega_{te}^J} \overline{F}_i d\Omega + \int_{\partial\Omega_{te}^J} \left[2\mu \left(\sum_{K=1}^{N} \Phi^{(K)}(\mathbf{X}) \hat{D}_{ij}^{\prime(K)} \right) n_j - \left(\sum_{K=1}^{N} \Phi^{(K)}(\mathbf{X})\, p^{(K)} \right) n_i \right] ds = 0. \tag{28}$$

At each node $\mathbf{X}_J$, Eqs. (28) represent 3 equations, in terms of the 7 variables $\hat{D}_{ij}^{\prime(J)}$ and $p^{(J)}$ at node $\mathbf{X}_J$, as well as the 7 variables $\hat{D}_{ij}^{\prime(K)}$ and $p^{(K)}$ at the other $(N-1)$ nodes $\mathbf{X}_K$ in the vicinity of $\mathbf{X}_J$.

When Eq. (20) is satisfied in a "strong-form" at each node $\mathbf{X}_J$, we obtain:

$$\sum_{K=1}^{N} \Phi^{(K)}(\mathbf{X}_J)\, \hat{D}_{kk}^{(K)} = 0, \tag{29}$$

which represents one constraint equation at each node $\mathbf{X}_J$, in terms of the variable $\hat{D}_{kk}^{(J)}$ at node $\mathbf{X}_J$, as well as the variables $\hat{D}_{kk}^{(K)}$ at the other $(N-1)$ nodes $\mathbf{X}_K$ in the vicinity of $\mathbf{X}_J$. When Eq. (20) is satisfied in a "strong-form" at each node $\mathbf{X}_J$, we obtain:

$$\sum_{K=1}^{N} \Phi^{(K)}(\mathbf{X}_J)\, \hat{D}_{kk}^{(K)} = \sum_{K=1}^{N} \Phi^{(K)}{}_{,i}(\mathbf{X}_J)\, \hat{v}_i^{(K)}, \quad (J = 1....N), \tag{30}$$

which represents N algebraic equations, relating the N unknowns $\hat{D}_{kk}^{\prime(J)}$ to the $3N$ unknowns $\hat{v}_i^{(J)}$. Thus $\hat{D}_{kk}^{(J)}$ can be solved in terms of $\hat{v}_i^{(J)}$, and when these are used in Eq. (29), we obtain one constraint equation at each node $\mathbf{X}_J$, in terms of the 3 unknowns $v_i^{(J)}$ at node $\mathbf{X}_J$, as well as the variables $v_i^{(K)}$ at each of the other $(N-1)$ nodes $\mathbf{X}_K$ in the vicinity of $\mathbf{X}_J$. When Eq. (21) is satisfied in a "strong-form" at each $\mathbf{X}_J$, using Eq. (24) and Eq. (25) in Eq. (21), we obtain:

$$\begin{aligned}\sum_{K=1}^{N}\Phi^{(K)}(\mathbf{X}_J)\hat{D}_{ij}^{\prime(K)} \equiv \frac{1}{2}\Bigg\{&\sum_{K=1}^{N}\left[\Phi^{(K)},_i(\mathbf{X}_J)\hat{v}_j^{(K)}\right]+\sum_{K=1}^{N}\left[\Phi^{(K)},_j(\mathbf{X}_J)\hat{v}_i^{(K)}\right]- \\ &\frac{2}{3}\left[\Phi^{(K)},_k(\mathbf{X}_J)\hat{v}_k^{(K)}\right]\Bigg\} \quad [i,j=1,2,3;\ J=1....N].\end{aligned} \tag{31}$$

Eq. (31) represent 6 constraint equations relating each of the 6 variables $D_{ij}^{\prime(J)}$ at each of the nodes $J=1...N$, to the $(3N)$ variables $v_i^{(J)}$ $[i=1,2,3;\ J=1...N]$. By solving Eq. (31) for each i,j=1,2,3, one may express $\hat{D}_{ij}^{\prime(J)}$ $(J=1...N)$ in terms of the $3N$ velocity variables $\hat{v}_i^{(J)}$. Thus the $6N$ variables $\hat{D}_{ij}^{\prime(J)}$ are expressed in terms of the $3N$ variables $\hat{v}_i^{(J)}$. When these $\hat{D}_{ij}^{\prime(J)}$ are used in Eq. (28), one obtains at each node $\mathbf{X}_J$, 3 equations in terms of the 4 variables ($\hat{v}_i^{(J)}$ and $\hat{p}^{(J)}$). These 3 equations, when coupled with the one constraint equations obtained at each node $\mathbf{X}_J$ through Eq. (29) and Eq. (30), represent the needed 4 equations to solve for the 4 variables $\hat{v}_i^{(J)}$ and $p^{(J)}$ at each node $\mathbf{X}_J$. It is interesting to observe that in the present method, the solution for $D_{kk}^{(J)}$ in Eq. (30), as well as for the solution of each $\hat{D}_{ij}^{\prime(J)}$ $(i,j=1,2,3)$ in Eq. (31), all in terms of $\hat{v}_k^{(J)}$, involve only the inversion of the non-singular [because of the nature of the MLS interpolation] $N\times N$ matrix $\Phi^{(J)}(\mathbf{X}_L)$. Since no Lagrange Multipliers, and no saddle-point type variational statements are involved either in the satisfaction of the incompressibility constraint, Eq. (19), or in the satisfaction of the constraint equations between mixed and primitive variables, Eqs. (20) and (21), there are no LBB conditions to be satisfied in the present MLPG Mixed-Finite-Volume Method. Instead, in the present method, Eqs. (19), (20) and (21), are all satisfied in a "strong-form" at every node $\mathbf{X}_K$, while Eqs. (18) are satisfied in a "finite-volume" type weak-form. In closing this Section 2, we note that the boundary conditions Eqs. (7) and (8) are satisfied in a "strong-form" (collocation), as discussed in Zhu, Zhang, and Atluri (1998), Atluri and Shen (2002a), Atluri and Shen (2002b), and Atluri (2004).

Another method that has been widely used to solve either the Stokes or the Navier-Stokes equations is the mesh-based finite volume method of Spalding (1972) and Patankar (1980). This numerical technique is a particular version of the method of global weighted residuals [Patankar (1980)]. The finite volume formulation is based on the use of a unit function as the test function, and the trial functions are commonly piecewise linear interpolation functions defined between the grid points (which are surrounded by a control volume). The mesh-based finite volume technique is based on the use of staggered grids (the velocity components are calculated at grid points that are staggered with respect to the grid points were pressure is computed) to ensure that the resulting system of equations is not singular, and to avoid the checkerboard pattern of the pressure field, however the mesh generation, particularly for complex 3D domains, is not trivial. In the finite volume approach of Spalding (1972) and Patankar (1980), the value of the flow variables and their spatial derivatives at the boundaries of the control volume, is determined by making assumptions about the spatial variation of the flow variables between the grid points (first and second-order upwind schemes, QUICK, power law, and Central differencing schemes, etc.). It is well-known that depending on the choice of the interpolation scheme, false diffusion can arise. Pressure-velocity coupling algorithms are used to obtain an equation for the pressure from the momentum and continuity equations. The most commonly used pressure-velocity coupling algorithm is the SIMPLE approach (and improved versions such as SIMPLER, SIMPLEC and PISO). The success of the pressure-velocity coupling algorithm depends on the correct formulation of the pressure equation in terms of "pressure corrections", which are functions of the mass imbalance at each finite volume. The finite volume also uses a segregated solution procedure, in which a sequential process is carried out to solve firstly an equation for a certain variable, then the equation for the next variable, etc. The SIMPLE algorithm (and improved versions) together with the segregated approach, constitute an iterative process that may lead to a converged solution of the problem. The use of the finite volume method of Spalding (1972) and Patankar (1980) for the solution fluid flow problems in systems with complex geometry are based on the formulation of the fluid equations in a generalized coordinate system. Even though the mesh-based finite volume method of Spalding (1972) and Patankar (1980) and the presently proposed novel meshless finite-volume mixed MLPG method, both have a unit function as a test function, it is clearly seen that they have fundamental differences, i.e. in the MLPG method: (i) the flow variables are calculated at the same nodes, (ii) there are no segregated or pressure-velocity coupling algorithms, (iii) there is no need to use interpolation schemes, such as QUICK, to calculate the value of the flow variables (or their derivatives) at the boundary of the local subdomain, (iv) an iterative process to get converged results is not necessary, (v) the trial functions can be of any order, and (vi) the solution of fluid flow problems with complex geometry can be formulated in a Cartesian coordinate system without the use of an isoparametric mapping or formulation of the fluid equations in a body fitted coordinate system.

3 Results and Discussion

Two cases of confined complex Stokes flows have been solved in this investigation. Complex Stokes flows exhibit *primary cells* (driven by a moving boundary) and *secondary cells* (driven by primary cells), and closed and separating streamlines, see Jana, Metcalfe, and Otino (1994). In this section we show the appropriateness of the present mixed-MLPG method coupled with a passive massless particle tracking algorithm (which is based on the MLS interpolation functions), to calculate the steady state velocity and pressure fields, and path lines (or stream lines) and vortex structures (*primary* and *secondary cells*) in the flow.

The first case under study, to be presented in Sect. 3.1, has an analytical solution, therefore it will be used to verify the accuracy of the proposed mixed MLPG-finite-volume method. The second case that is presented in Sect. 3.2 does not possess an analytical solution, therefore the pressure and velocity fields can only be obtained by numerical computations or by experimental techniques. The second case is a variant of the vortex mixing flow geometry proposed by Jana, Metcalfe, and Otino (1994), and Price, Mullin, and Kobine (2003). Whereas the previous flow geometry consists of three coaxial circular cylinders, two of smaller diameter inside a third, our new flow geometry consists also of three coaxial cylinders, but the external cylinder has an elliptical cross-section. In the previous studies, the outer circular cylinder rotates about its axis, with constant angular velocity (hence the tangential velocity on the surface of the outer cylinder, that drives the flow, is also a constant). However in our new vortex mixing flow, the outer elliptical cylinder does not rotate about its axis, but its wall slides with a constant angular velocity, hence the tangential velocity that drives the internal flow, is a function of the polar radius of the ellipse.

3.1 Stokes flow between eccentric rotating cylinders

Numerical simulations of the Stokes flow in the annular region between two coaxial infinitely long circular cylinders, induced by the independent uniform rotation of one, or both of the cylinders about their axes (which do not coincide with each other), are presented in this section. We carry out the comparison between the numerical results and the analytical solution given by Ballal and Rivlin (1976).

The physical problem is shown in Fig. 2 together with a typical distribution of the MLPG nodes used to represent the solution domain. The inner and outer cylinders are of radius r_2 and r_1, respectively, with the distance between the centers of the cylinders is given by the eccentricity e. The outer cylinder can rotate about its own axis with an angular speed ω_1, either counter-clockwise or clockwise, while the inner cylinder always rotates around its own axis clockwise with an angular

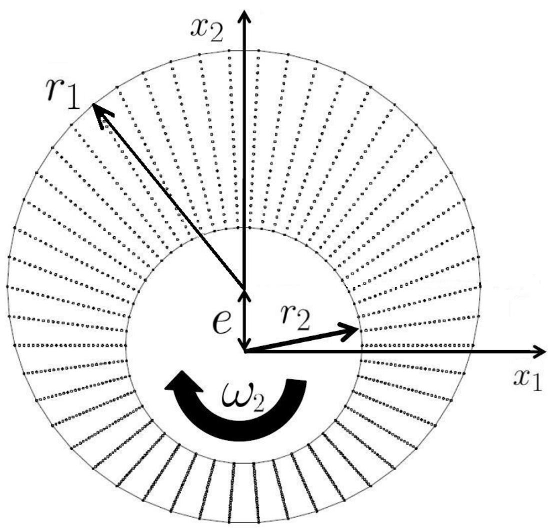

Figure 2: Stokes flow between eccentric rotating cylinders. The circular housing rotates at angular speed ω_1 and the inner cylinder rotates at angular speed ω_2. The characteristic length scale of the housing is l=r_1, the relevant parameters are: the aspect ratio A=r_1/r_2, the eccentricity ratio ε=$e/(r_1-r_2)$ and the angular speed ratio $\hat{\omega}$=ω_2/ω_1. A typical MLPG nodes distribution is also shown.

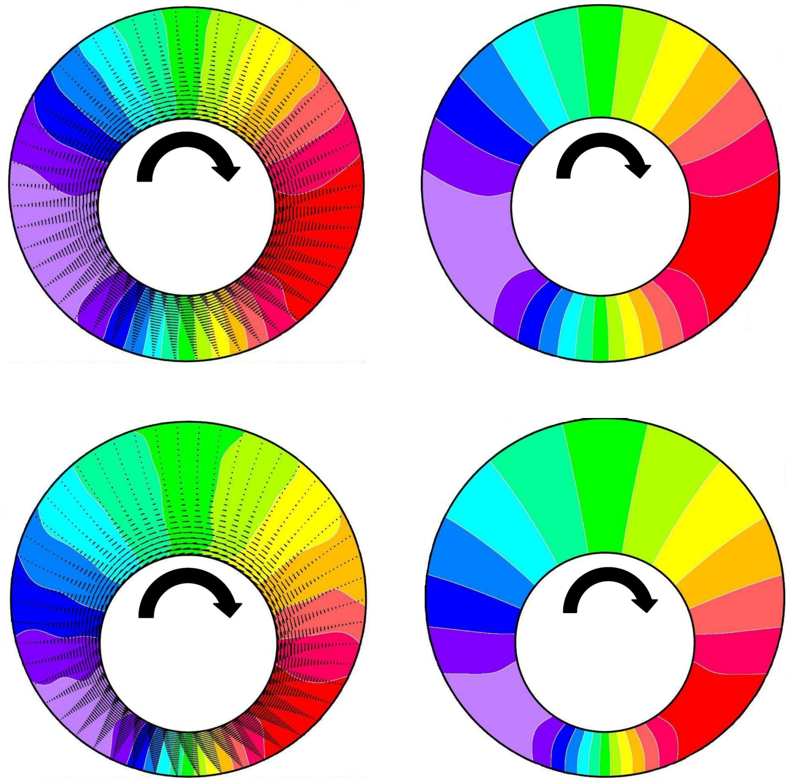

(A)

(B)

velocity ω_2. The relevant parameters of the system are the aspect ratio A=r_1/r_2, the eccentricity ratio $\varepsilon = e/(r_1 - r_2)$ and the angular speed ratio $\hat{\omega} = \omega_2/\omega_1$. In the numerical experiments we keep the aspect ratio fixed to $A = 2$, while the eccentricity ratio ε acquires the values: 0.26, 0.5 and 0.7. For the cases with ε=0.26 and ε=0.7, the outer cylinder was kept stationary (i.e. $\hat{\omega} = \infty$), while for the case with ε=0.5, the angular speed ratio $\hat{\omega}$ has the values: ∞, 0.25 and -0.25. The positive sign means that the outer cylinder rotates clockwise, while the negative sign indicates that the outer cylinder rotation is counter-clockwise.

Fig. 3 shows the pressure isocontours as a function of the eccentricity ratio ε and the angular speed ratio $\hat{\omega}$. Left column shows the mixed-MLPG results, whereas right column displays the analytical solution. It is clearly observed that the mixed-MLPG method provides a pressure field that does not show the typical chessboard distribution that is obtained by those numerical algorithms that calculate the unknown variables of the flow at the same location (non-staggered nodes distribution) and use the same polynomial expansion for the pressure and velocity fields. It is important to remark that by using the novel mixed-MLPG method, an itera-

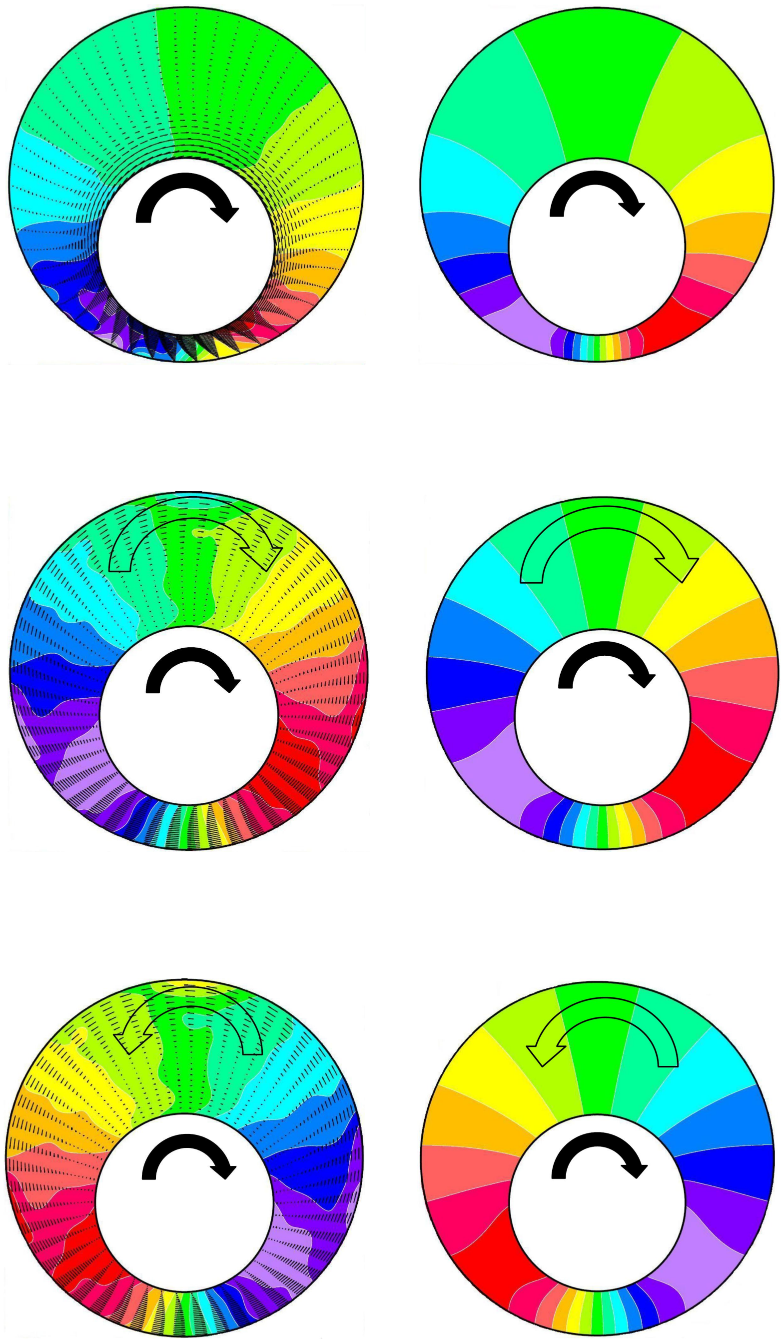

(C)

(D)

(E)

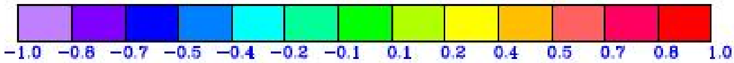

Figure 3: Stokes flow between eccentric rotating cylinders. Dimensionless isocontours of the pressure field. For all the cases the aspect ratio is fixed to A=2, and the number of MLPG nodes is equal to 1250. The pressure is normalized with respect to the maximum pressure in the flow domain. Left column: mixed-MLPG method results, the dimensionless velocity vectors are also shown. Right column: analytical results [Ballal and Rivlin (1976)]. (A) ε=0.26 and $\hat{\omega}$=∞. (B) ε=0.5 and $\hat{\omega}$=∞. (C) ε=0.7 and $\hat{\omega}$=∞. (D) ε=0.5 and $\hat{\omega}$=0.25. (E) ε=0.5 and $\hat{\omega}$=-0.25.

tive (segregated) process (like SIMPLE-family algorithms) is not required to obtain the correct pressure field. Figs. 3(A) and 3(B), show that the agreement between the mixed-MLPG results and the analytical solution, reported by Ballal and Rivlin (1976), is successful and encouraging. Fig. 3(C) shows that in the small gap region, some deviations from the analytical solution are observed. However in the wide gap region it can be seen that the agreement is also successful. Figs. 3 (A)-(C) show that due to the clockwise rotation of the inner cylinder, pressure begins to increase from the widest gap region to the small gap region (along the clockwise direction, or for positive x_1 values). Note that as the ε value is increased, the region with higher pressure moves towards the smallest gap region, and becomes smaller. Due to symmetry conditions, the same behaviour shows the region with lower pressure, i.e. from the widest gap region to the small gap region, along the counter-clockwise direction (for negative x_1 values), it moves towards the smallest gap region, and becomes smaller. Figs. 3(D) and 3(E), show the cases for co-rotating and counter-rotating cylinders, respectively (see the large arrow indicating the rotation of the outer cylinder). Fig. 3(E) shows that due to the counter-clockwise rotation of the outer cylinder, the region with highest pressure is located on the negative side of the x_1-axis. Note that in the wide gap region the results are also encouraging. The main reason for disagreement between the numerical results and the analytical solution, particularly in the small gap region for ε=0.7, see Fig. 3 (C), is because the accuracy of the results provided by the MLPG method strongly depends on the definition of two length scales. The first one is called the domain of support (or size of the support) of the weight function used in the MLS interpolation scheme. The second length scale is the size (radius) of the local sub-domain (i.e. support of the local Heaviside step test function domain) enclosing every sample node (see Atluri and Shen (2002b) and Atluri and Shen (2002a), for a detailed description of the two length scales). In this study, both length scales are calculated in terms of the average

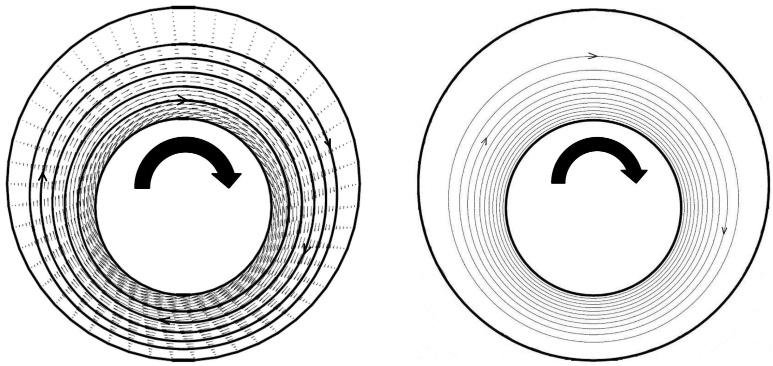

(A)

distance $\overline{h}$ (a constant value) between the MLPG nodes in the flow domain. In the results we show in Fig. 3, the average distance $\overline{h}$ is obtained by taking into account all the nodes in the flow. Hence if the distance between the nodes is almost uniform, as is the case with ε=0.26 or ε=0.5, the accuracy of the results only depends on the values of the two length scales in terms of the constant $\overline{h}$. However, if the nodes are distributed not uniformly (high concentration of nodes in the small gap region and low concentration of nodes in the wide gap region), as is the case when ε=0.7, the accuracy of the results will also depend on the spatial variation of the two length scales (spatial variation of the local average distance between the nodes). Research work at the Center for Space Research and Education at UCI, is being conducted to find (besides the rate of convergence, and error estimation studies of the novel mixed-MLPG method) the optimal choice of the two length scales for the solution of the Stokes problem with complex geometry and non-uniform nodes distribution. The results we present in Fig. 3 were preceded by several numerical computations in which in order to obtain MLPG results which are independent of the number of nodes used, tests were carried out from 625 nodes (25 nodes along the radial direction and 25 nodes along the angular direction) to 1250 nodes (25 nodes along the radial direction and 50 nodes along the angular direction). In all the cases displayed in Fig. 3, the size of support of the weight function is calculated as $2.65\overline{h}$, while the size of support for the test function is given by $0.5\overline{h}$.

Fig. 4 shows the streamline patterns, generated by tracking the orbit of massless fluid elements (right column), and the analytical stream functions (left column, with arrows indicating the flow direction). The selected time increment Δt used to numerically solve the dynamical equations of a Lagrangian tracer, determines the number of calculated locations along its orbit. On the average 1×10^6 fluid element positions were calculated to generate a closed streamline, as it is shown on the left column of Fig. 4. The velocity of the fluid at the instantaneous location of the

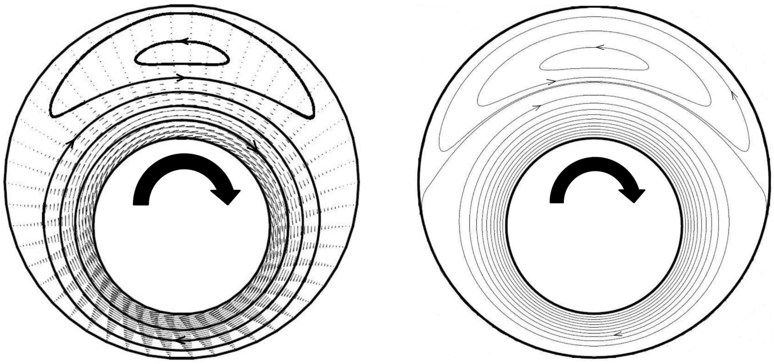

(B)

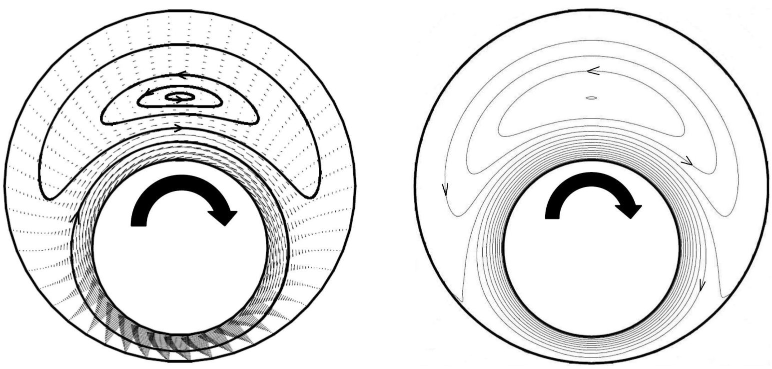

(C)

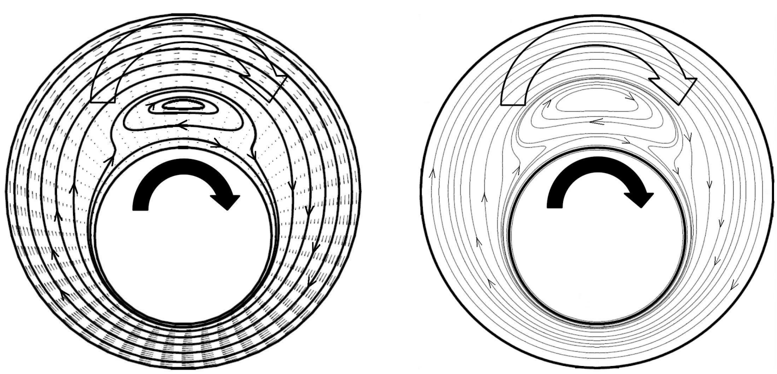

(D)

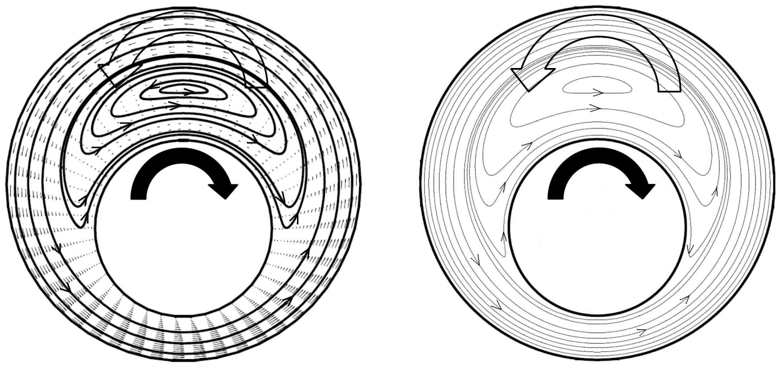

(E)

Figure 4: Stokes flow between eccentric rotating cylinders. The aspect ratio is fixed to A=2. Left column: mixed-MLPG method results, path lines (or streamlines) generated by following the orbit of passive massless fluid elements, velocity vectors are also shown. Right column: Stream function analytical results [Ballal and Rivlin (1976)] with arrows indicating the flow direction. (A) ε=0.26 and $\hat{\omega}=\infty$. (B) ε=0.5 and $\hat{\omega}=\infty$. (C) ε=0.7 and $\hat{\omega}=\infty$. (D) ε=0.5 and $\hat{\omega}$=0.25. (E) ε=0.5 and $\hat{\omega}$=-0.25.

passive tracer is calculated by using the MLS interpolation technique. It is observed in Fig. 4 that the complex Stokes flow exhibits secondary cell motion that is driven by contact with primary cells. Fig. 4 (A) shows that for ε=0.26, no flow separation occurs on the outer cylinder. However, Fig. 4 (B) shows that for ε=0.5, separation takes place on the outer boundary (see the pair of parabolic critical points on the stationary outer surface in the analytical solution). It has been analytically found that when A=2, no separation occurs for $\varepsilon < 0.32424$, this confirm our findings. Note that Figs. 4 (A)-(C), correspond to Figs. 18 (a), (c) and (d) of Ballal and Rivlin (1976)'s paper. Right panel of Fig. 4 (C) also shows the pair of parabolic critical points on the stationary outer surface. It is seen that when the external cylinder is stationary, the only stagnation point in the interior of the fluid, exists on the x_2-axis (centre of the vortex, or elliptic critical point), this is a theoretical finding. Figs. 4 (D) and (E), show the streamlines when the cylinders rotate in the same direction and when they rotate in opposite directions, respectively. Note the large arrow indicating the sense of rotation of the outer cylinder. Fig. 4 (D) shows that due to both the geometrical configuration (A and ε values) and the angular speed ratio $\hat{\omega}$, of the system under study, only one interior stagnation point occurs at the centre of the vortex (on the x_2-axis). Fig. 4 (D) resembles Fig. 14 (b) of Ballal and Rivlin (1976)'s paper, i.e. without intersection of the streamlines and no interior critical hyperbolic points. In Fig. 4 (E) we observe that the only stagnation point lies on the x_2-axis, (centre of the vortex), this is also a theoretical finding. It

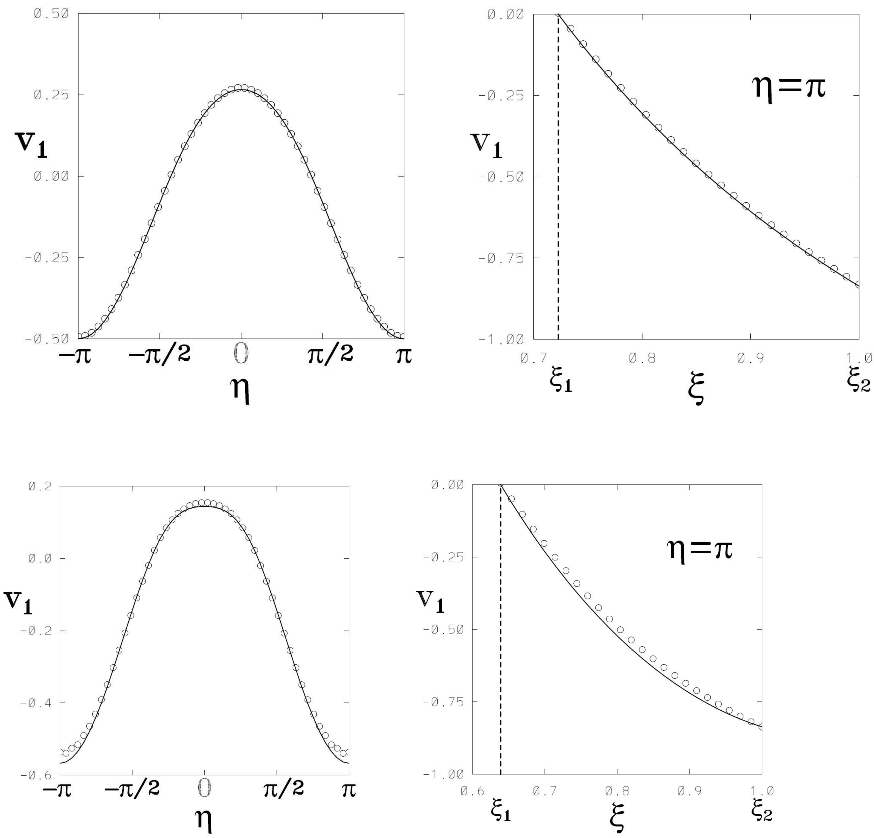

(A)

(B)

is clearly observed in Fig. 4 that the numerical results and the analytical solution are in successful agreement.

Fig. 5 shows the v_1 velocity component as a function of the bipolar coordinates (ξ and η), in which is formulated the analytical solution [Ballal and Rivlin (1976)]. The coordinate $\xi = \xi_1$ corresponds to the surface of the outer cylinder, while the coordinate $\xi = \xi_2$ represents the surface of the inner cylinder. The coordinate η is measured from the region of largest gap (η=0), to π (clockwise direction, or positive x_1), and to $-\pi$ (counter-clockwise direction, or negative x_1). Left column of Fig. 5 shows the v_1 velocity component evaluated at the circle $\xi = (\xi_1+\xi_2)/2$ as a function of the variable η (from -π to π). It is observed in Figs. 5 (A) and 5(B) that when the external housing is stationary, and when ε=0.26 and ε=0.5, the agreement is satisfactory. Notice that due to the clockwise rotation of the inner cylinder the highest positive v_1 value is located at the largest gap region ($\eta = 0$), whereas the highest negative v_1 value is located at the smallest gap region ($\eta = \pm\pi$). Left

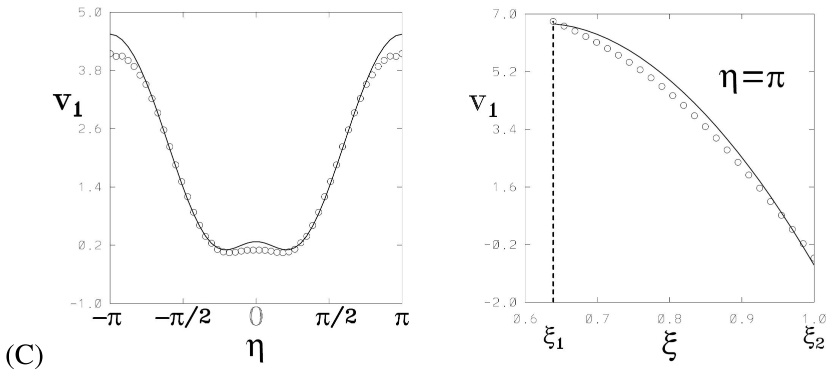

Figure 5: Stokes flow between eccentric rotating cylinders. Dimensionless v_1 velocity component as a function of the bipolar coordinates (ξ, η). Left column $v_1(\eta)$ at the location $(\xi_1+\xi_2)/2$. Right column $v_1(\xi)$ at the smallest gap region i.e. at η=π. Continuous line: Analytical results [Ballal and Rivlin (1976)]. Circles: mixed-MLPG method results. (A) ε=0.26 and $\hat{\omega}$=∞. (B) ε=0.5 and $\hat{\omega}$=∞. (C) ε=0.5 and $\hat{\omega}$=-0.25.

panel of Fig. 5 (C) shows that the numerical solution follows the trend of the analytical results when the cylinders counter-rotate. A discrepancy is observed at the smallest gap location ($\eta=\pm\pi$) and at the widest gap location (η=0). It is observed that due to the highest value of the counter-clockwise angular speed of the outer cylinder ($\hat{\omega}=-0.25$), and due to the vortex formation at the largest gap region, see Fig. 4 (E), v_1 always remains positive with largest value at the small gap region. Right column of Fig. 5 shows at the smallest gap region ($\eta=\pi$) the v_1 velocity component from the outer cylinder ξ_1 to the inner cylinder ξ_2 (note that the variable ξ has been normalized with respect to the ξ_2 value). It is observed that when the outer cylinder is stationary, and for ε=0.26 and ε=0.5, see Figs. 5 (A) and (B), the agreement is successful. However when a counter-rotation between both cylinders occurs, a small difference is observed in the middle region $0.7\le\xi\le0.9$, see Fig. 5 (C). Right column of Figs. 5 (A) and (B) show that at $\xi=\xi_1$, the velocity v_1 is zero, and due to the clockwise rotation of the inner cylinder, v_1 becomes negative and acquires the tangential negative v_1 velocity of the internal cylinder (at $\xi=\xi_2$). It is observed in Fig. 5 (C) that due to the counter-clockwise rotation of the outer cylinder, v_1 is positive from $\xi=\xi_1$ to $\xi\approx0.97$. Beyond this value v_1 becomes negative and acquires the tangential negative speed of the inner cylinder at $\xi=\xi_2$. It is convenient to mention that in order to perform the comparison between the analytical solution (obtained in a bipolar coordinate system (ξ, η)) and the numerical results (obtained in a Cartesian coordinate system), firstly the

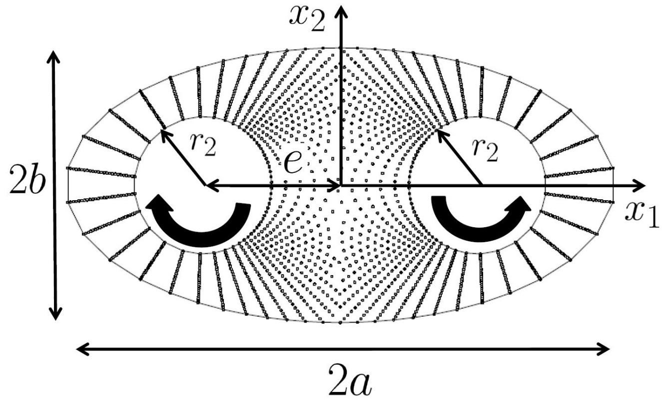

Figure 6: Stokes vortex mixing flow in the space bounded by two inner independently rotating circular cylinders, and an elliptical housing whose wall slides at constant angular speed ω_1. The characteristic length scale of the housing is l=a. See the text for the definition of the relevant parameters. A typical MLPG nodes distribution is also shown.

bipolar coordinate system was mapped to a Cartesian coordinate system by using the transformation rules given by Ballal and Rivlin (1976) (see Eqs. (3.1) of their paper), and secondly a rotation and translation was performed in order to obtain the analytical results in our Cartesian coordinate system, whose origin is located at the centre of the inner cylinder, see Fig. 2.

After showing the agreement between the results provided by the mixed MLPG method and the analytical solution, we may say that the novel numerical algorithm can be used to calculate with enough accuracy the background velocity (and pressure) field, that is used to advect passive fluid elements in creeping flows. In the next section we show that the calculation of trajectories of Lagrangian passive fluid elements, will conduct to the study of vortex structures and critical points that exhibit our new vortex flow mixer.

3.2 A new complex Stokes flow

The physical problem is shown in Fig. 6. The fluid fills the space between the outer channel with elliptical cross section and two inner circular cylinders of equal radii r_2. The centres of the inner cylinders are located along the major diameter of the outer channel and are set symmetrically (a distance e) about the center of the ellipse. The relevant parameters of the system, such as the aspect ratio $A = a/b$, the confining aspect ratio $c = r_2/b$, the eccentricity ratio $\varepsilon = e/a$ and the angular speed ratio $\hat{\omega} = (\omega_{2r} + \omega_1)/\omega_{2l}$ (where ω_{2l} and ω_{2r} are the angular velocities of the inner left and right cylinders respectively, and ω_1 is the angular speed of the elliptical sliding wall) can be selected to tune the flow topology. In this paper we select to vary the forcing parameter $\hat{\omega}$, whereas the geometrical parameters are kept fixed to the values A=2, c=0.5 and ε=0.5. In the analyzed cases, the outer cylinder can slide its wall either counter-clockwise or clockwise; the right inner cylinder can also rotate counter-clockwise or clockwise; however the left inner cylinder always rotates clockwise with the same fixed angular velocity ω_{2l}. Table 1 shows the values of the forcing parameter $\hat{\omega}$ for the fifteen cases under study. In Table 1 the definition of the angular speed direction of the cylinders is as follows: C-ω_{2l} means that the angular speed of the left inner cylinder is clockwise, CC-ω_{2r} means that the angular speed of the right inner cylinder is counter-clockwise, and CC-ω_1 means that the angular speed of the sliding wall of the ellipse is counter-clockwise.

Table 1: Forcing parameter $\hat{\omega} = (\omega_{2r} + \omega_1)/\omega_{2l}$ in the Stokes vortex mixing flow. CC means counter-clockwise direction and C means clockwise direction of the cylinders angular speed.

Case	CC-ω_1	$\omega_1 = 0$	C-ω_1
A (C-ω_{2l}, CC-ω_{2r})	-1.5	-1	-0.5
B (C-ω_{2l}, C-ω_{2r})	0.5	1	1.5
C (C-ω_{2l}, ω_{2r}=0)	-0.5	0	0.5
D (C-ω_{2l}, CC-ω_{2r})	-1	-0.5	0
E (C-ω_{2l}, C-ω_{2r})	0	0.5	1

In this section we show the velocity and pressure fields provided by the novel mixed-MLPG method in terms of the forcing parameter $\hat{\omega}$. The topology of the streamlines (generated by following the orbit of massless fluid elements) is also shown. Pressure gradient vectors and velocity vectors along the trajectory of fluid elements enclosing internal critical points are also presented. We also show that at a given internal critical point, the eigenvalues of the Jacobian matrix **J** satisfy the dynamical systems theory. In a 2-D flow field, the two eigenvalues of a hyperbolic critical point are real numbers with $R_1 \times R_2 < 0$ (a positive value refers to repulsion, while a negative value refers to attraction), whereas the two eigenvalues of an elliptic critical point are imaginary numbers with I_1=-I_2. Our findings confirm the accuracy of the computed pressure and velocity fields obtained by the novel mixed-MLPG method.

Figs. 7 and 8 show the dimensionless pressure field contours together with the velocity vectors, and the topology of the streamlines respectively, for the cases

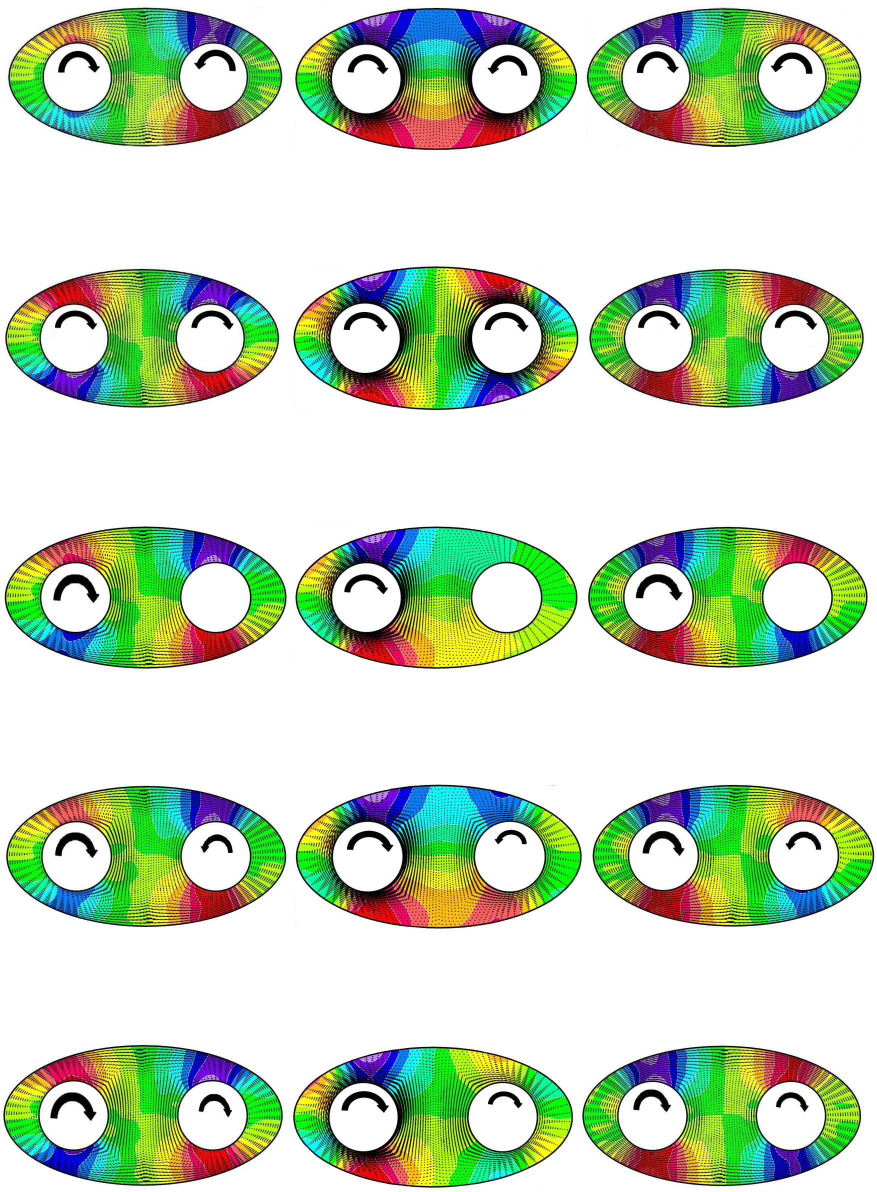

(A)

(B)

(C)

(D)

(E)

Figure 7: Dimensionless pressure distribution and velocity vectors in the Stokes vortex mixing flow. Number of MLPG nodes is equal to 2890. The pressure field is normalized with respect the maximum pressure in the flow domain. See Table 1 for the definition of columns and rows.

described in Table 1. Note that there is a direct correspondence between the rows and columns of Table 1 and the rows and columns of Figs. 7 and 8. It is clearly observed that by using the mixed-MLPG method, the pressure distribution does not show a chessboard behaviour. For case A, the angular speed of the inner cylinders is the same but with opposite directions, therefore ω_{2r}=-ω_{2l} (by convention we have defined clockwise direction as positive, while counter-clockwise direction as negative). For case B, ω_{2r}=ω_{2l}. For case C, ω_{2r}=0. For case D, ω_{2r}=-$\omega_{2l}/2$. And for case E, ω_{2r}=$\omega_{2l}/2$. In all cases, the angular speed of the outer elliptical cylinder is either ω_1=-$\omega_{2l}/2$, ω_1=0, and ω_1=$\omega_{2l}/2$, see Table 1. Due to the elliptical geometry of the outer cylinder, the sliding wall tangential velocity that drives the fluid, is a function of the polar radius of the ellipse. In Cartesian coordinates the x_1 and x_2 components of the tangential velocity of points located at the sliding wall are given as

$$v_1 = -\frac{b}{a}x_2\omega_1 \quad \text{and} \quad v_2 = \frac{a}{b}x_1\omega_1, \tag{32}$$

where a and b are the semi-major and semi-minor axes of the ellipse respectively, and x_1 and x_2 are the coordinates of the points along the elliptical cylinder, see Fig. 6. Fig. 7 shows that due to the viscous stresses generated by driving fluid into the converging regions, all the cases exhibit the highest and lowest values of the pressure in the small gap regions (theory of lubrication).

Left column of Fig. 7 shows that for counter-rotating inner left cylinder and external cylinder (see rows (A)-(E)), in the small gap region, a reduction of the highest and lowest values of the pressure, with respect to the pressure in the small gap region around the right cylinder (except row (B) which shows symmetry conditions), is observed. Due to the counter-flowing streams and to the small pressure drop, a vortex with center on the x_1 axis is formed close to the inner left cylinder, near the negative semi-major axis a, see left column of Fig. 8 rows (A)-(E). Left column of Fig. 7 shows that for co-rotating inner right cylinder and external cylinder, see rows (A) and (D), due to both co-flowing streams and high pressure drop in the small gap region, no vortex is created near the positive semi-major axis a, see left column of Fig. 8 rows (A) and (D). Left column of Fig. 7 also shows that for counter-rotating inner right cylinder and external cylinder see rows (B) and (E), due to the shear stress generation by the counter-flowing streams, a vortex is created with center on the x_1 axis and near the positive semi-major axis a, see left column of Figs. 8 rows (B) and (E). For zero speed angular velocity of the inner right cylinder, see left column of Fig. 7, row (C), due to the high pressure drop in the small gap region, no vortex is created near the positive semi-major axis a, see left column of Fig. 8 row (C). Right column of Fig. 7 shows that for co-rotating inner left cylinder and external cylinder, the pressure pattern around the left cylinder, is independent of

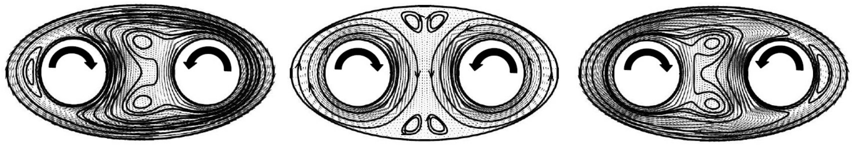

(A)

the right cylinder rotation, see rows (A)-(E). The corresponding streamlines shown on right column of Fig. 8, confirm the fact that around the inner left cylinder (rotating always clockwise), in the small gap region, the streamlines are similar in all cases, see rows (A)-(E). Right column of Fig. 7 shows that for counter-rotating inner right cylinder and external cylinder (see rows (A), (C) as a special case, and (D)), the pressure drop is reduced with respect to the pressure conditions around the left cylinder. Due to the combined effects of counter-flow and low pressure drop, a vortex with center on the x_1 axis appears in the neighbourhood of the inner right cylinder, near to the positive semi-major axis a, see right column of Fig. 8, rows (A), (C), (D). On the other hand for co-rotating inner right cylinder and external cylinder (see right column, rows (B) and (E), of Figs. 7 and 8), due to the combined effects of co-flowing streams and high pressure drop, in the small gap region vortices are not observed.

The central column of Figs. 7 and 8, shows the results for ω_1=0. As the angular speed of the left inner cylinder is a constant, the results show the effect of rotation of the inner right cylinder on the pressure pattern and topology of the streamlines. Due to the boundary conditions and the geometry of the mixer, in the small gap region no vortices are generated when ω_1=0. Fig. 7 shows that in the central region of the mixer (widest region), the pressure field acquires intermediate values with small pressure gradients that lead to the formation of critical points, as it is shown in Fig. 8. The streamlines shown in Fig. 8 have been generated by calculating 5×10^5 locations of a lagrangian tracer along each closed orbit. The topology of the streamlines shows that hyperbolic as well as elliptic critical points occur in the flow field. In Fig. 8, it is possible to observe hyperbolic critical points on left and central columns, row (B), on left and central columns, row (C), on left column, row (D), and on left and central column, row (E)). Whereas elliptic points occur in almost all the cases, with the exception of rows (B)-(E) with ω_1=0 (central column). The critical points we show in Fig. 8 probably are not the only ones, because on regions of small velocity, flow structures may be present.

Fig. 9 shows the velocity vector (left column) and the negative pressure gradient vector (right column) at points located along closed streamlines for two cases: case (B) with C-ω_1 (top row) and case (C) with CC-ω_1 (bottom row). Panel on the left column, top row shows that as the streamline encloses an elliptic critical point, its

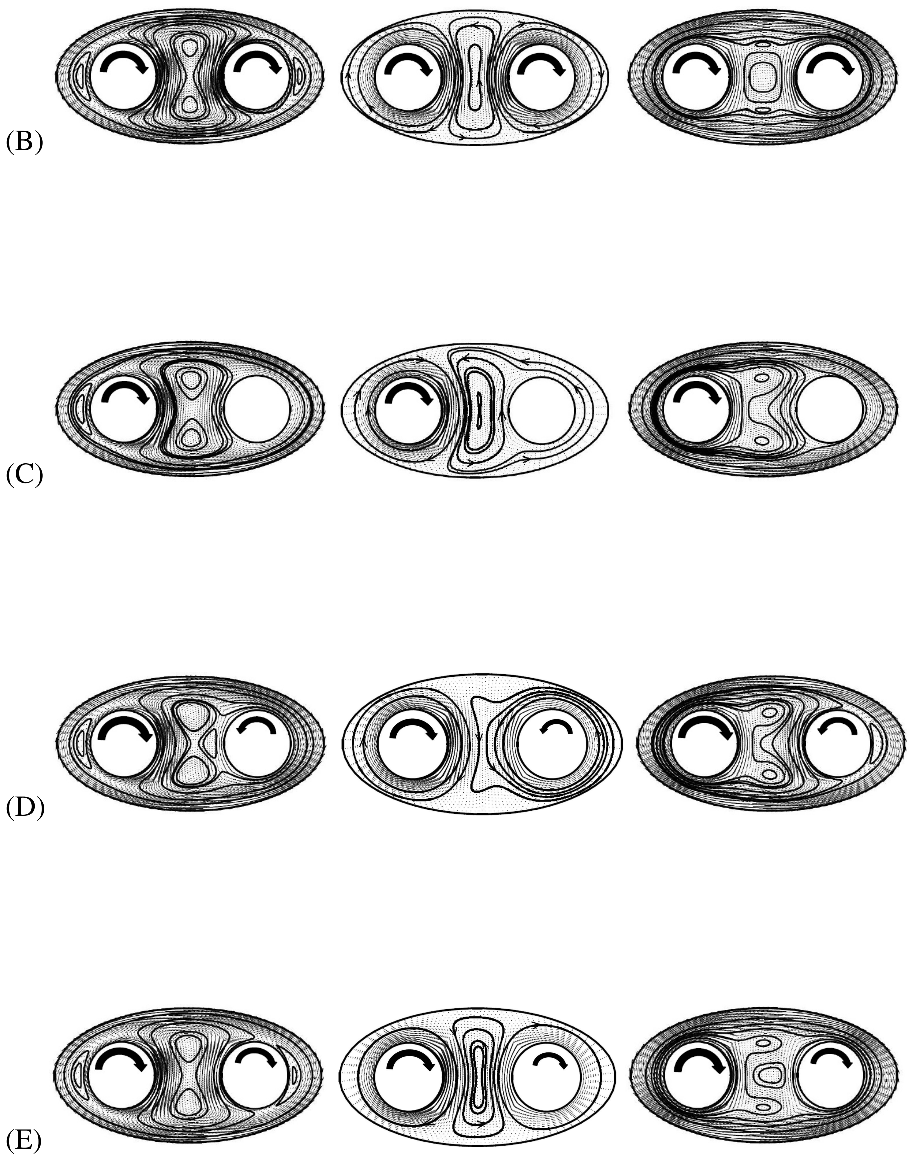

Figure 8: Stokes vortex mixing flow streamlines with fixed geometry and variable forcing parameter $\hat{\omega}$ as it is specified by Table 1. Number of MLPG nodes is equal to 2890.

(B) 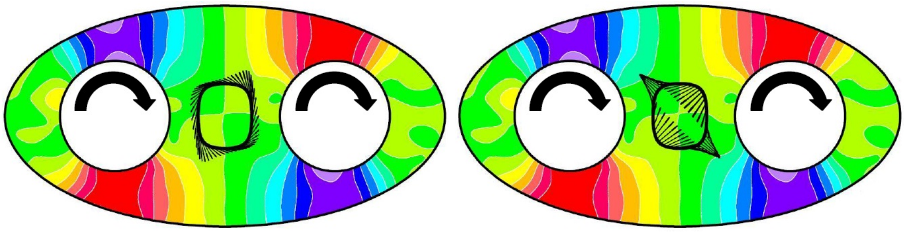

Poincaré index is equal to 1, see the corresponding case on Fig. 8. Panel on the left column, bottom row shows that as the streamline encloses one hyperbolic point (with Poincaré index equal to -1), and two elliptic points (with Poincaré index equal to 1), its Poincaré index is equal to 1, see the corresponding case on Fig. 8. Panels on the right column (top and bottom rows) show that the negative pressure gradient vector allows to identify the pressure forces that balance the viscous stresses, acting on the fluid element along its orbit. Panels on the right column clearly show the regions of repulsive and attracting forces that characterize not only the behaviour of streamlines converging into a saddle (hyperbolic) critical point, but also, in this case, the behaviour of streamlines surrounding an elliptic critical point. Panels on the right column also show that by travelling counter-clockwise once along the streamline, and counting the number counter-clockwise revolutions made by the negative pressure gradient vector with its base on the streamline and its head pointing in the direction of the negative gradient, it is found that its " Poincaré index" is -1, as is the case of a streamline enclosing a saddle point, with repulsion and attraction features. To the knowledge of the authors a detailed topological skeleton of the pressure gradient vector field in active mixers with two inner cylinders has not been reported in the literature. Previous studies on chaotic advection have been mostly based on the topological skeleton of the velocity vector field.

Finally, we have evaluated the eigenvalues of the Jacobian matrix $\mathbf{J}$

$$\mathbf{J} = \begin{vmatrix} \frac{\partial v_1}{\partial x_1} & \frac{\partial v_1}{\partial x_2} \\ \frac{\partial v_2}{\partial x_1} & \frac{\partial v_2}{\partial x_2} \end{vmatrix}, \tag{33}$$

at the elliptic critical point enclosed by the streamline shown in Fig. 9 top row (see also Fig. 8 (B) right column), and at the critical points (one hyperbolic and two elliptic) enclosed by the the streamline shown in Fig. 9 bottom row (see also Fig. 8 (C) left column).

Table 2, shows the eigenvalues of the Jacobian matrix. It is observed that for the elliptic critical points (ECP), the real part of the complex numbers is much smaller than the imaginary part, hence the critical points represent a vortex center. On the

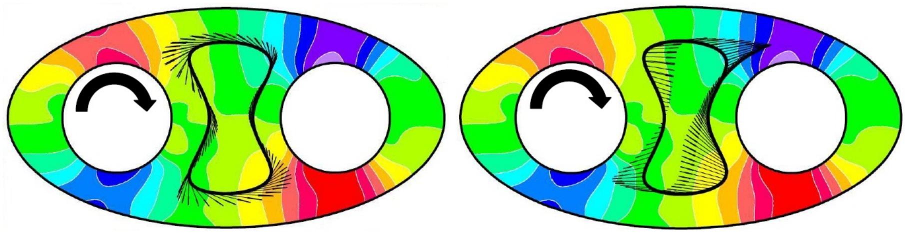

(C)

Figure 9: Complex Stokes vortex mixing flow. Top row: case (B) with C-ω_1. Bottom row: case (C) with CC-ω_1, see Fig. 8 and Table 1. Left column velocity vectors along a closed streamline. Right column: negative pressure gradient vectors along a closed streamline.

Table 2: Eigenvalues of the Jacobian matrix $\mathbf{J}$ at the critical points enclosed by the streamlines shown in Fig. 9. ECP means elliptical critical point. HCP means hyperbolic critical pont. Numbers within parenthesis are the dimensionless coordinates x_1 and x_2 of the critical point. R_1 and R_2 are real numbers. I_1 and I_2 are imaginary numbers.

Case	R_1	R_2	I_1	I_2
B (C-ω_{2l}, C-ω_{2r}, C-ω_1). ECP(0,0)	2×10^{-6}	2×10^{-6}	4.5	-4.5
C (C-ω_{2l}, ω_{2r}=0, CC-ω_1). HCP(0,0)	8.4	-8.4	0	0
C (C-ω_{2l}, ω_{2r}=0, CC-ω_1). ECP(-0.02,-0.25)	3.5×10^{-4}	3.5×10^{-4}	10.4	-10.4
C (C-ω_{2l}, ω_{2r}=0, CC-ω_1). ECP(-0.02,0.25)	-3.6×10^{-4}	-3.6×10^{-4}	10.4	-10.4

other hand, Table 2 shows that for the hyperbolic critical point (HCP) the imaginary part of the complex number is zero. Our findings confirm the fact that by using the novel mixed-MLPG method the velocity field at internal critical points, satisfies the nonlinear systems theory.

4 Conclusions

A novel MLPG Mixed finite-volume method, based on meshless independent interpolations for the velocity vector, the deviatoric velocity strain tensor, the volumetric velocity strain tensor and the pressure field, has been presented to calculate the pressure and velocity fields in steady state complex Stokes flows. This method does not involve any LBB conditions, and the computed pressure field is smooth and does not suffer from the malady of a checkerboard pattern. The comparison between the analytical solution and the results provided by the novel mixed method for the case of eccentric circular cylinders was excellent. The numerical simulation of a new complex Stokes vortex mixing flow shows that complex flow patterns are generated that may lead to mixing enhancement of highly viscous fluids. The velocities, and the spatial derivatives of the velocity and pressure fields, at points along the orbits of massless tracers, have been successfully interpolated by using the MLS numerical technique. The mixed-MLPG method can be used to verify results provided by theoretical approaches aimed to identify in a simple way the critical points in the flow domain. We propose to use the mixed-MLPG method to obtain the topological skeleton of the pressure gradient vector field in steady state complex Stokes flows.

Acknowledgment: Financial support for this investigation was provided by DGAPA-UNAM (Sabbatical leave and research stay of R. Avila at the Center for Aerospace Research & Education, University of California, Irvine) and DGSCA-UNAM through the Visualization Observatory (Ixtli project). Most of the computations were carried out on the supercomputer of DGSCA-UNAM and on the Linux-based 'BDUC' cluster at the University of California, Irvine. The third author's research was supported by the World Class University (WCU) Program, through the National Research Foundation of Korea, funded by the Ministry of Science & Technology (Grant No. R33-10049) during his visits to Pusan National University.

References

Anderson, P. D.; Ternet, D.; Peters, G. W. M.; Meijer, H. E. H. (2006): Experimental/numerical analysis of chaotic advection in a three-dimensional cavity flow. *Intern Polymer Processing*, vol. 21, pp. 412–420.

Aref, H. (1984): Stirring by chaotic advection. *J. Fluid Mechanics*, vol. 143, pp. 1–21.

Aref, H. (2002): The development of chaotic advection. *Physics of Fluids*, vol. 14, pp. 1315–1325.

Aref, H.; Balachandar, S. (1986): Chaotic advection in a Stokes flow. *Physics of Fluids*, vol. 29, pp. 3515–3521.

Atluri, S. N. (2004): *The Meshless Methods (MLPG) For Domain & Bie Discretizations*. Tech Science Press.

Atluri, S. N.; Han, Z. D.; Rajendran, A. M. (2004): A new implementation of the meshless finite volume method, through the MLPG "Mixed approach". *CMES: Computer Modeling in Engineering & Sciences*, vol. 6, pp. 491–513.

Atluri, S. N.; Shen, S. (2002): *The Meshless Local Petrov-Galerkin (MLPG) Method*. Tech Science Press.

Atluri, S. N.; Shen, S. (2002): The Meshless Local Petrov-Galerkin (MLPG) method: A simple & less-costly alternative to the Finite Element and Boundary Element methods. *CMES: Computer Modeling in Engineering & Sciences*, vol. 3, pp. 11–51.

Atluri, S. N.; Zhu, T. (1998): A new Meshless Local Petrov-Galerkin (MLPG) approach in computational mechanics. *Computational Mechanics*, vol. 22, pp. 117–127.

Ballal, B. Y.; Rivlin, R. S. (1976): Flow of a Newtonian fluid between eccentric rotating cylinders: intertial effects. *Arch. Rational Mech. Anal.*, vol. 62, pp. 237–294.

Bratianu, C.; Atluri, S. N. (1983): A Hybrid finite element method for Stokes flow: Part I-formulation and numerical studies. *Computer Methods in Applied Mechanics and Engineering*, vol. 36, pp. 23–37.

Brezzi, F.; Fortin, M. (1991): *Mixed and Hybrid Finite Element Methods*. Springer-Verlag.

Chaiken, J.; Chevray, R.; Tabor, M.; Tan, Q. M. (1986): Experimental study of Lagrangian turbulence in a Stokes flow. *Proc. R. Soc. Lond. A*, vol. 408, pp. 165–174.

Chaiken, J.; Chu, C. K.; Tabor, M.; Tan, Q. M. (1987): Lagrangian turbulence and spatial complexity in a Stokes flow. *Physics of Fluids*, vol. 30, pp. 687–694.

Hwang, W. R.; Anderson, P. D.; Hulsen, M. A. (2005): Chaotic advection in a cavity flow with rigid particles. *Physics of Fluids*, vol. 17, 043602.

Jana, S. C.; Metcalfe, G.; Otino, J. M. (1994): Experimental and computational studies of mixing in complex Stokes flows: the vortex mixing flow and multicellular cavity flows. *J. Fluid Mechanics*, vol. 269, pp. 199–246.

Kang, T. G.; Hulsen, M. A.; Anderson, P. D.; den Toonder, J. M. J.; Meijer, H. E. H. (2007): Chaotic advection using passive and externally actuated particles in a serpentine channel flow. *Chemical Engineering Science*, vol. 62, pp. 6677–6686.

Karniadakis, G.; Beskok, A.; Aluru, N. (2005): *Microflows and Nanoflows: Fundamentals and Simulation*. Springer.

Lin, H.; Atluri, S. N. (2000): Meshless Local Petrov Galerkin (MLPG) method for convection-diffusion problems. *CMES: Computer Modeling in Engineering & Sciences*, vol. 1, pp. 45–60.

Lin, H.; Atluri, S. N. (2001): The Meshless Local Petrov-Galerkin (MLPG) method for solving incompressible Navier-Stokes equations. *CMES: Computer Modeling in Engineering & Sciences*, vol. 2, pp. 117–142.

Metcalfe, G.; Lester, D.; Ord, A.; Kulkarni, P.; Rudman, M.; Trefry, M.; Hobbs, B.; Regenaur-Lieb, K.; Morris, J. (2010): An experimental and theoretical study of the mixing characteristics of a periodically reoriented irrotational flow. *Proc. R. Soc. Lond. A*, vol. 368, pp. 2147–2162.

Patankar, S. V. (1980): *Numerical heat transfer and fluid flow*. Hemisphere Publishing Co.

Price, T. J.; Mullin, T.; Kobine, J. J. (2003): Numerical and experimental characterization of a family of two-roll-mill flows. *Proc. R. Soc. Lond. A*, vol. 459, pp. 117–135.

Shankar, P. N.; Kidambi, R. (2009): Mixing in internally stirred flows. *Proc. R. Soc. Lond. A*, vol. 465, pp. 1271–1290.

Spalding, D. B. (1972): A novel finite difference formulation for differential expressions involving both first and second derivatives. *International Journal for Numerical Methods in Engineering*, vol. 4, pp. 551–559.

Stremler, M. A.; Haselton, F. R.; Aref, H. (2004): Designing for chaos: applications of chaotic advection at the microscale. *Phil. Trans. R. Soc. Lond. A.*, vol. 362, pp. 1019–1036.

Wang, J.; Feng, L.; Otino, J. M.; Lueptow, R. (2009): Inertial effects on chaotic advection and mixing in a 2D cavity flow. *Ind. Eng. Chem. Res.*, vol. 48, pp. 2436–2442.

Ying, L. A.; Atluri, S. N. (1983): A Hybrid finite element method for Stokes flow: Part II-stability and convergence studies. *Computer Methods in Applied Mechanics and Engineering*, vol. 36, pp. 39–60.

Zhu, T.; Zhang, J. D.; Atluri, S. N. (1998): A local boundary integral (LBIE) method in computational mechanics, and a meshless discretization approach. *Computational Mechanics*, vol. 21, pp. 223–235.